

Changes in migration mode of brine and supercritical CO₂ in imbibition process under steady flow state of very slow fluid velocities

Tetsuya Kogure,^{*} Yi Zhang, Osamu Nishizawa[†] and Ziqiu Xue

CO₂ Storage Research Group, Research Institute of Innovative Technology for the Earth, Kizugawa, Kyoto 619-0292, Japan. E-mail: kogure@riko.shimane-u.ac.jp

Accepted 2018 May 23. Received 2018 May 15; in original form 2018 January 26

SUMMARY

Relative permeability curves and flow mechanisms of CO₂ and brine in Berea sandstone were investigated during a two-phase flow imbibition process, where CO₂ saturation in the rock decreased from 55 to 9 per cent by stepwise decrease of CO₂/brine injection ratios. Total fluid flow velocity was $4.25 \times 10^{-6} \text{ m s}^{-1}$, corresponding to the capillary number of order $\sim 10^{-8}$ for CO₂ flow. The relative permeability curves showed a slight hysteresis compared to those during the drainage process. Local CO₂ saturation and the differential pressure showed temporal fluctuations when the average differential pressure showed constant values or very small trends. The fluctuations in local CO₂ saturation correlate with local porosity distributions. The differential pressure between the inlet and outlet ends showed the largest fluctuation when the CO₂/brine ratio equals to one. A final brine-only injection resulted in more CO₂ trapped within low-porosity zones. These results suggest important roles of ganglion dynamics in the low flow rate ranges, where fluid pathways undergo repetitive brine snap-off and coalescence of CO₂ ganglia that causes morphological changes in distributions of CO₂ pathways.

Key words: Permeability and porosity; Hydrogeophysics; Image processing.

1 INTRODUCTION

It is important to study two-phase flow mechanisms of CO₂ and brine to establish a scientific basis for CCS (Carbon Capture and Storage) technologies. In practice, the actual CO₂ flow velocities at field CCS sites are very low when considering the spatial expansion of reservoirs and associated long-term fluid migrations. Since reservoirs generally contain geologic heterogeneity in both the vertical and the lateral directions (Ito *et al.* 2017), fluid migration crossing heterogeneity is also important. The flow in a reservoir is deemed to be a two-phase flow of CO₂ and brine because the displaced brine also flows away from the injection well. When conducting laboratory experiments for studying flow of the fluids in reservoirs, it is therefore important to focus on low flow velocity injections and the flow direction across the rock heterogeneities. However, there have been few experimental studies of CO₂/brine concurrent injection at very low flow velocities in porous rocks. Also, most experiments have been within homogeneous rock samples or with

flow not crossing internal rock heterogeneity boundaries. We recently reported results of a low flow velocity CO₂/brine concurrent injection experiment during a drainage process of two-phase flow crossing rock heterogeneity, where CO₂ saturation increases with increasing of CO₂/brine injection rates (Kogure *et al.* 2017). This study is a continuation of that previous experimental study under the same low flow velocity conditions.

Pore-scale displacement processes between wetting and non-wetting fluids in porous media under low flow velocity or low capillary numbers have been recently explained by ganglion dynamics revealed by microscopic observations employing synchrotron-beam micro X-ray computerized tomography (CT) (μ CT; e.g. Rücker *et al.* 2015; Armstrong *et al.* 2016; Singh *et al.* 2017). The observations show the nature of the morphological change in flow paths in the capillary-dominated regime, where ganglion dynamics play important roles. The major mechanisms of ganglion dynamics are snap-off by brine and coalescence of non-wetting fluids. These studies require us to recast the conventional understanding about immiscible two-fluid flow in porous media (Singh *et al.* 2017), which has been described using relative permeability curves (RPC) and by implicitly assuming independent pathways for the two fluids (Pini & Benson 2013). Ganglion dynamics is more applicable than conventional Darcy-flow approximations in that it works for capillary displacements of fluids and morphological changes in flow pathways in which percolation is involved.

^{*} Now at: Department of Geoscience, Interdisciplinary Graduate School of Science and Engineering, Shimane University, Matsue, Shimane 690-8504, Japan.

[†] Now at: Public Works Research Institute, Tsukuba, Ibaraki 305-8516, Japan.

A synchrotron-beam μ CT provides images with extremely high resolution that can reveal capillary pressures of non-wetting fluids at each pore (Singh *et al.* 2017), which helps to understand the mechanisms of pore-scale migration between wetting and non-wetting fluids. It is therefore, important to exploit the new findings for better understanding of two-phase flow at core scale where the saturation process of wetting and non-wetting fluids in pore networks is the major concern. Because most of the synchrotron-beam μ CT experiments have been conducted under low-capillary-number conditions, the results of core-scale flow experiments under low-capillary-number conditions should be interpreted on the basis of ganglion dynamics. Kogure *et al.* (2017) reported that ganglion dynamics works in core-scale CO_2 /brine drainage displacements under low flow velocity conditions ($8.67 \times 10^{-6} \text{ m s}^{-1}$), where supercritical CO_2 pathway in a Berea sandstone core underwent morphological changes. There are strong relationships between the inlet-outlet differential pressure and the morphological changes of CO_2 pathways estimated from medical X-ray images. The experiments revealed that core-scale inhomogeneity affects formations of pathways, which were referred to as channelled pathway or randomly distributed pathway having different roles in CO_2 transport in porous rocks. The relationship between the fluids saturation and the nominal permeabilities were explained by the percolation threshold of pore networks in sandstones.

We continued the two-phase flow experiments of the brine- CO_2 system throughout an imbibition process, where brine and CO_2 were co-injected by increasing the brine ratio under the same experimental settings. We discuss here different trapping mechanisms between the capillary trapping during two-phase flow and the residual gas trapping after the final brine-only injection, in terms of local porosity distributions. The conventional RPC values for the low-capillary-number two-phase flow and its hysteresis are also presented.

2 METHODS

The specimen was a cylindrical core of Berea sandstone with a diameter of 35 mm and a length of 70 mm. The core has a layered structure with high- and low-porosity layers perpendicular to the core axis (Fig. 1). Absolute permeability, k_{abs} , was $3.1 \times 10^{-14} \text{ m}^2$ (31 mD) at a confining pressure of 12 MPa and mean fluid pressure of 10 MPa. The bulk porosity was 17.5 per cent, which corresponds to a sample pore volume of 11.8 mL.

Since the experiment was continued after the drainage experiment described by Kogure *et al.* (2017), all the experimental settings and environmental conditions were the same as shown in the previous study: 40 °C temperature, and about 10 and 12 MPa pore pressure and confining pressure, respectively. These ensure that CO_2 was in a supercritical phase everywhere in the assembled flow system.

In drainage, six injection experimental runs denoted as D1–D6 were previously performed (Table 1), with the brine/ CO_2 ratios 9:1, 7:3, 5:5, 3:7, 1:9 and 0:10, respectively. Imbibition was started after run D6, where the brine saturation, S_b , for the entire core (an area of the axial distance $d = 5\text{--}65 \text{ mm}$ for excluding image artefacts) was 44.9 per cent. Imbibition experiments were performed for the brine/ CO_2 ratios 1:9, 3:7, 5:5, 7:3, 9:1 and 10:0, denoted as runs I1–I6, respectively (Table 1). Total flow rate of brine and CO_2 was set at 0.50 mL min^{-1} , corresponding to a flow velocity of $8.67 \times 10^{-6} \text{ m s}^{-1}$. The injection duration times ranged from 472.2 (run I5) to 1956.6 min (run I6).

Saturation of brine and CO_2 (S_b and S_{CO_2}) was determined by a medical X-ray CT scanner. The data were used to calculate relative permeability with Darcy's equation. A medical X-ray CT scanner (Aquilion ONE TSX 301A, Toshiba Medical Systems Corp.) was used to image the core between 5 and 65 mm from the fluid inlet side. The reconstructed voxel size was $0.78 \times 0.78 \text{ mm}$ for the slices perpendicular to the core axis and 0.5 mm for the axis direction. The following equations yield the porosity, ϕ , and the degree of CO_2 saturation, S_{CO_2} , based on the voxel CT (Hounsfield) numbers (Akin & Kovscek 2003):

$$\phi = \frac{\text{CT}_{\text{brine}}^{\text{sat}} - \text{CT}^{\text{dry}}}{\text{CT}_{\text{brine}} - \text{CT}_{\text{air}}}, \quad (1)$$

$$S_{\text{CO}_2} = c (\text{CT}_{\text{obs}} - \text{CT}_{\text{brine}}^{\text{sat}}) = \frac{\text{CT}_{\text{obs}} - \text{CT}_{\text{brine}}^{\text{sat}}}{\text{CT}_{\text{CO}_2}^{\text{sat}} - \text{CT}_{\text{brine}}^{\text{sat}}}, \quad (2)$$

where $\text{CT}_{\text{brine}}^{\text{sat}}$, $\text{CT}_{\text{CO}_2}^{\text{sat}}$, CT^{dry} and CT_{obs} are the voxel CT numbers of a scanned rock which is saturated with brine, CO_2 , vacuumed and other conditions observed during the scan, respectively. CT_{brine} and CT_{air} are the CT numbers for the single brine or air phase, respectively, and c is the coefficient that relates S_{CO_2} to the difference in CT number between the scan for the experimental run in question and the scan run for the brine-saturated core. To plot RPC, the saturation value S_{CO_2} for the rock sample at each steady state was obtained from the smoothed average of the distributions during 2 hr before the end of measurements.

Relative permeability is calculated using Darcy's law:

$$Q_i = -\frac{A k_{\text{abs}} k_{ri}}{\mu_i} \frac{\Delta P}{L} \quad (i = \text{brine or } \text{CO}_2), \quad (3)$$

where Q_i and μ_i are the flow rate ($\text{m}^3 \text{ s}^{-1}$) and the viscosity (Pa s) of each fluid, k_{abs} and k_{ri} are the absolute permeability (m^2) and the relative permeability, A and L are the sectional area (m^2) and the length of the core (m), and P is the differential pressure across the core (Pa). The values of μ_b and μ_{CO_2} at 40 °C and 10 MPa are $6.53 \times 10^{-4} \text{ Pa s}$ (Wagner & Kretschmar 2008) and $4.78 \times 10^{-5} \text{ Pa s}$ (Span & Wagner 1996), respectively.

We used the measured P , ignoring the capillary pressure gradient in CO_2 . We consider that the CO_2 saturation values in rock do not necessarily reflect the local CO_2 capillary pressures in two-fluid flow conditions. We also ignored the capillary end effect that appears as an offset pressure in the measured capillary pressure difference. In any case, the corrections due to capillary entry pressure in Berea sandstone, *ca.* 5–6 kPa (Pini & Benson 2013), are considered to be small compared to the observed pressure differences, 35–120 kPa. Detailed discussions on these issues are given in Kogure *et al.* (2017).

3 FLUCTUATIONS IN SATURATION AND DIFFERENTIAL PRESSURE

Fig. 2 shows saturation maps of brine (CO_2) just before the end of each experimental run. The saturation maps are illustrated for the four vertical cross-sections: the upper panel is a cross-section along the long axis of the specimen and the lower panels are perpendicular to the long axis at the designated axial positions. The distribution of CO_2 appears to be controlled by the sedimentary structure of the specimen, which is characterized by high-porosity layers (HPL) and low-porosity layers (LPL; Fig. 1). A high CO_2 saturated zone between 5 and 25 mm from the inlet was due to blocking of CO_2 flow by the LPL located at 25 mm. We separated the core into two zones at $d = 25 \text{ mm}$, by referring to these as a stuck zone and a

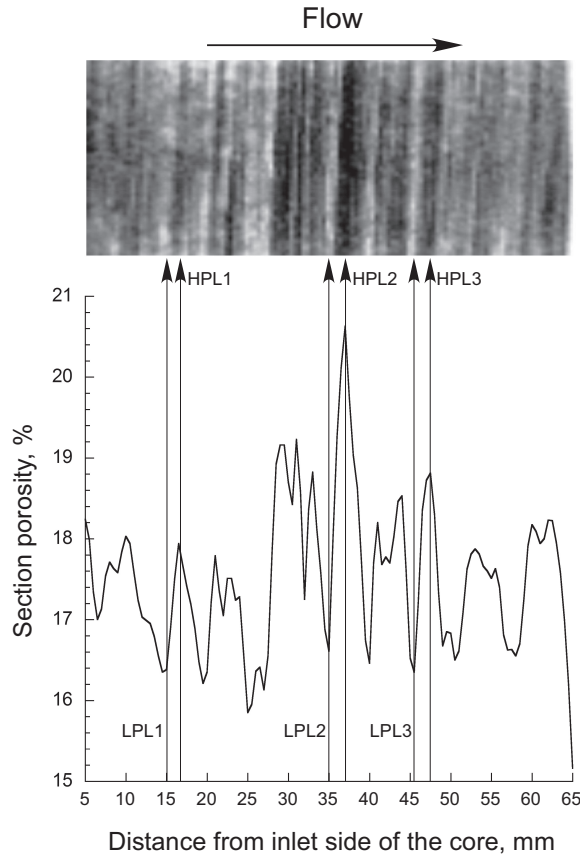


Figure 1. X-ray CT image of the Berea sandstone core used in this study and average porosity profile along the core axis (Kogure *et al.* 2017). Lateral scales in the image and the graph correspond to each other.

Table 1. Summary of observations in drainage (Kogure *et al.* 2017) and imbibition.

| Run no. | Flow rate (mL min ⁻¹) | | | Injected volume (mL) | | | S _b (per cent) | S _{CO₂} (per cent) | S _b (per cent) | S _{CO₂} (per cent) | S _b (per cent) | S _{CO₂} (per cent) | ΔP (kPa) | k _{rb} | k _{rCO₂} |
|--------------------------------------|-----------------------------------|-----------------|-------|----------------------|-----------------|--------|---------------------------|--|---------------------------------|--|---------------------------|--|----------|-----------------|------------------------------|
| | Brine | CO ₂ | Total | Brine | CO ₂ | Total | Entire core (d = 5–65 mm) | Stuck zone (d = 5–25 mm) | Normal-flow zone (d = 25–65 mm) | | | | | | |
| <i>Drainage (Kogure et al. 2017)</i> | | | | | | | | | | | | | | | |
| D1 | 0.45 | 0.05 | 0.50 | 473.9 | 56.8 | 530.6 | 63.4 | 36.6 | 59.3 | 40.7 | 65.4 | 34.6 | 88.3 | 0.130 | 0.001 |
| D2 | 0.35 | 0.15 | 0.50 | 343.0 | 149.6 | 492.6 | 60.9 | 39.1 | 57.6 | 42.4 | 62.6 | 37.4 | 99.6 | 0.090 | 0.002 |
| D3 | 0.25 | 0.25 | 0.50 | 340.8 | 340.2 | 681.0 | 57.4 | 42.6 | 53.9 | 46.1 | 59.2 | 40.8 | 84.8 | 0.075 | 0.005 |
| D4 | 0.15 | 0.35 | 0.50 | 412.9 | 961.0 | 1373.9 | 56.9 | 43.1 | 51.7 | 48.3 | 59.6 | 40.4 | 55.5 | 0.069 | 0.010 |
| D5 | 0.05 | 0.45 | 0.50 | 63.5 | 546.5 | 610.0 | 52.2 | 47.8 | 46.6 | 53.4 | 55.0 | 45.0 | 35.2 | 0.036 | 0.020 |
| D6 | 0.00 | 0.50 | 0.50 | 0.0 | 452.9 | 452.9 | 44.9 | 55.1 | 36.8 | 63.2 | 49.1 | 50.9 | 6.7 | 0.000 | 0.116 |
| <i>Imbibition (this study)</i> | | | | | | | | | | | | | | | |
| I1 | 0.05 | 0.45 | 0.50 | 63.1 | 546.2 | 609.3 | 50.8 | 49.2 | 45.4 | 54.6 | 53.5 | 46.5 | 37.6 | 0.033 | 0.018 |
| I2 | 0.15 | 0.35 | 0.50 | 71.6 | 168.6 | 240.2 | 53.9 | 46.1 | 48.9 | 51.1 | 56.5 | 43.5 | 73.2 | 0.053 | 0.008 |
| I3 | 0.25 | 0.25 | 0.50 | 126.5 | 128.5 | 255.0 | 54.9 | 45.1 | 49.8 | 50.2 | 57.4 | 42.6 | 84.1 | 0.075 | 0.005 |
| I4 | 0.35 | 0.15 | 0.50 | 167.2 | 73.1 | 240.3 | 56.3 | 43.7 | 50.5 | 49.5 | 59.3 | 40.7 | 107.9 | 0.083 | 0.002 |
| I5 | 0.45 | 0.05 | 0.50 | 210.4 | 25.6 | 236.0 | 56.9 | 43.1 | 51.3 | 48.7 | 59.8 | 40.2 | 115.8 | 0.100 | 0.001 |
| I6 | 0.50 | 0.00 | 0.50 | 978.3 | 0.0 | 978.3 | 90.1 | 9.9 | 89.8 | 10.2 | 90.2 | 9.8 | 16.4 | 0.772 | 0.000 |

Note: d = distance from inlet side of the core.

normal-flow zone for 5 < d < 25 and 25 < d < 65 mm, respectively. Saturation of CO₂ is generally higher in the stuck zone than in the normal-flow zone. Fig. 2 shows a gradual decrease in S_{CO₂} during runs I1–I5 with the CO₂ distribution pattern changing slightly with

decreasing S_{CO₂} over the entire core. Saturation of CO₂ decreases drastically at the end of run I6. The values of S_b at the end of runs I1–I6 for the entire core (d = 5–65 mm) were 50.8, 53.9, 54.9, 56.3, 56.9 and 90.1 per cent, respectively (Table 1).

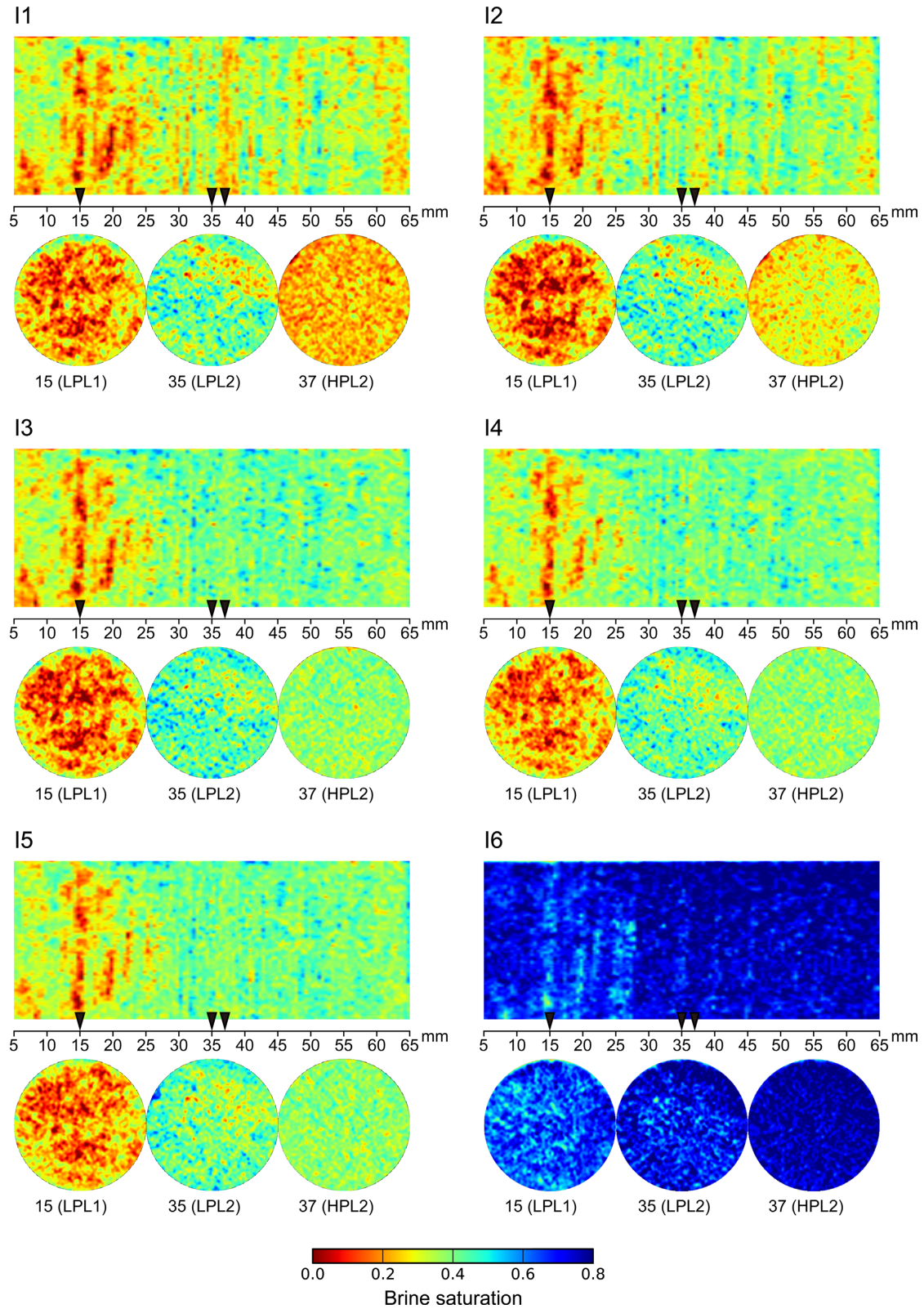


Figure 2. Saturation maps of brine and sectional S_{CO_2} profiles along the long axis during the injection of CO_2 in runs I1–I6. The black triangles on the horizontal axis show the locations of axial images.

Fig. 3 shows the changes in S_{CO_2} and differential pressure across the core, ΔP , against the injected brine content for the runs I1–I6. Fig. 4 shows time variations of ΔP for 5 hr before the end of injections. Although the experimental runs were continued for 8–32 hr (depending on brine/ CO_2 injection ratio), the small trends of ΔP in runs I2 and I3 still remained. It would not have been practical to continue the experimental runs much longer since the character of changes in ΔP was already essentially stabilized. Fig. 5 shows temporal changes in the axial distribution of S_{CO_2} for a 2 hr period prior to the end of injection runs except for the run I6 (1 hr). The observed fluctuations in ΔP and S_{CO_2} persisted for as long as the co-injection was continued. The plotted values of ΔP in Fig. 3 were obtained from the regression lines in Fig. 4 at the end of each run, and S_{CO_2} were obtained by averaging the fluctuating values for 1 or 2 hr before the end of runs. We believe that the fluctuations in ΔP and S_{CO_2} reflect important mechanisms of the two-phase flow as discussed below.

Large fluctuation amplitudes were found in runs I3 and I4 for both S_{CO_2} and ΔP . The runs I3 and I4 also showed remarkable fluctuations in local S_{CO_2} values when approaching steady states. For the one-phase flow run, I6, the distribution of S_{CO_2} was close to convergence in this period. In two-phase flow runs, I1–I5, the range of average S_{CO_2} is 40.2–46.5 per cent in the normal-flow zone.

We consider that the fluctuation in the S_{CO_2} distribution is a characteristic phenomenon, particularly in low flow velocity injection with flow direction crossing the sedimentation layers. The oscillatory fluctuations in the S_{CO_2} distribution, especially in the normal-flow zone, can be explained by considering intermittent connection and disconnection of CO_2 percolation clusters by coalescences of CO_2 clusters and snapped off events due to brine invasion into the critical paths of the CO_2 percolation clusters (Kogure *et al.* 2017).

The maximum fluctuation in S_{CO_2} and ΔP appears in run I3 in both the stuck and normal-flow zones. The equal flow rate of CO_2 and brine in run I3 may have created the largest number of snap-off and coalescence of CO_2 clusters, leading to the most prominent morphological changes of CO_2 pathways.

4 CHANGES IN FLOW PROCESSES DUE TO DECREASING OF S_{CO_2}

The fluctuation amplitude in S_{CO_2} in each run distinguishes runs I1 and I2 (0.851 and 1.46×10^{-2}) from runs I3, I4 and I5 (4.41 , 2.79 and 1.90×10^{-2}), indicated by the 2σ range bars in Fig. 3. The fluctuation in S_{CO_2} is recognized as the results of morphological changes in CO_2 pathways for drainage (Kogure *et al.* 2017). To confirm the effect of pathway changes on the fluctuation in S_{CO_2} for imbibition, changes in saturation distribution were analysed from sectional CT images. Fig. 6 shows time-differential images of S_{CO_2} in the runs I2 and I3, representing the difference in S_{CO_2} between images taken at the beginning of each measurement run and at the noted specific time prior to the end of the measurements. When estimating the volume from the section images, the images for run I3 show the migration of a larger volume of brine and CO_2 than run I2, suggesting more changes in pathway occupation between brine and CO_2 in run I3 than in run I2. The changes frequently occur particularly in HPL in the normal-flow zone by intermittent displacements between CO_2 and brine in pores.

Fig. 7 shows axial profiles of average S_{CO_2} for each cross-section perpendicular to the core axis (hereafter, we call this the S_{CO_2} axial profile) in the last drainage run D6 and imbibition runs I1–I6. The values were obtained at the end of each measurement. Note that run

I6 was 100 per cent brine injection. The average S_{CO_2} in the normal-flow zone gradually decreased as the runs proceeded from run D6 to I3, and became almost uniform around 40 per cent from run I3 to I5. This 40 per cent saturation value is close to the saturation value required to form percolated ganglia in sandstones (e.g. Argaud *et al.* 1989; Han *et al.* 2009). This suggests that development of effective CO_2 pathways during imbibition is also governed by percolated ganglia. The percolation threshold of 40 per cent saturation also appears to be the same for both drainage and imbibition.

For the normal-flow zone, the S_{CO_2} in runs D6–I2 is mostly larger than 40 per cent (Fig. 7), whereas in runs I3–I5 it distributed around 40 per cent. Therefore, more percolated ganglia are expected in runs D6–I2 than in runs I3–I5, because even a small increment in S_{CO_2} slightly over the percolation threshold can increase the density of percolated CO_2 ganglia. The percolated ganglia will act as a channel for CO_2 flow. Since brine saturation S_b exceeds the percolation threshold (40 per cent) in all measurement runs, there could be many pathways for each fluid in runs D6–I2. This will cause small ΔP and its fluctuation because of small disturbance of CO_2 flow by brine and vice versa (Figs 3 and 4). On the other hand, percolation clusters of CO_2 may become unstable due to the increase of brine snap-off against CO_2 clusters caused by the increase of brine flow rate in runs I3–I5 where S_{CO_2} is around the percolation threshold. Isolated CO_2 ganglia that are surrounded by brine-filled pores or pore throats may then coalesce again with the CO_2 percolation clusters (Rücker *et al.* 2015). Thus, CO_2 pathways are updated with morphological changes. The repetitive snap-off and coalescence of CO_2 ganglia lead to the changes in location and alignment of fluid pathways. Since the saturation value of brine exceeds the percolation threshold in all imbibition runs, isolated CO_2 ganglia may hamper the channel flow of brine by increasing effective tortuosity. The S_{CO_2} values in runs I4 and I5 maintained a value close to the percolation threshold with continuous snap-off and coalescence.

It is interesting to note that the local fluctuations in S_{CO_2} appear in areas larger than core inhomogeneity (Fig. 6). In this co-injection experiment, CO_2 blobs and brine were co-injected through 0.5 mm diameter stainless tubes. Zhang *et al.* (2017) made an independent experiment to observe CO_2 blobs and brine flowing through an X-ray-transparent plastic tube of 0.5 mm inner diameter, under the same pressure and temperature conditions as this study. The volume of each injected CO_2 blob was smaller than 0.01 mL under the equal flow rate of CO_2 and brine, which is less than the pore volume of each imaged slice. This may suggest that the local S_{CO_2} fluctuations resulted from movements of large CO_2 ganglia grown inside the rock sample by coalescences.

5 RESIDUAL CO_2 TRAPPING

In the axial profiles of S_{CO_2} (Fig. 7), a positive correlation exists between the peaks and troughs of S_{CO_2} and porosity variations in the normal-flow zone (e.g. LPL2–HPL2 and LPL3–HPL3), except for run I6 (100 per cent brine imbibition), where S_{CO_2} corresponds to the residual CO_2 remaining in low-porosity zones. In the stuck zone, S_{CO_2} was not correlated with porosity (e.g. LPL1–HPL1).

The positive correlation between the axial profile of S_{CO_2} and porosity has been reported and discussed in Perrin & Benson (2010) for the drainage process. However, CO_2 distribution in run I6 shows a reverse correlation in which the trapped residual CO_2 concentrates

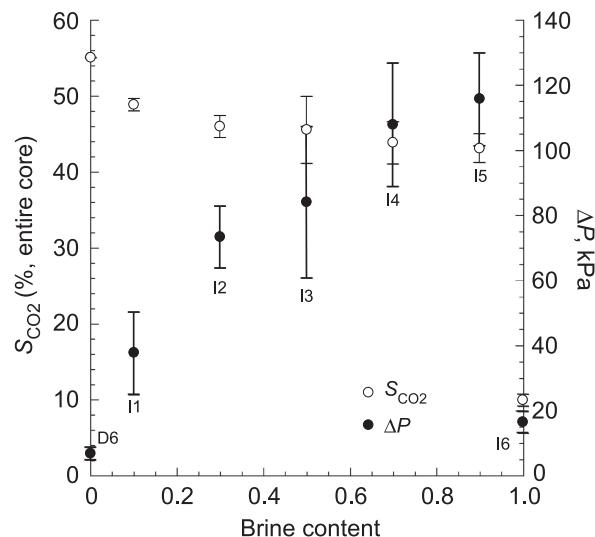


Figure 3. Steady-state CO_2 saturation values (S_{CO_2}) and differential pressure between inlet and outlet of the core (ΔP) with respect to injected brine volume ratio. All experimental runs were conducted at constant flow rate of 0.5 mL min^{-1} . Each bar shows the range of 2σ of fluctuation amplitudes relative to the mean for both S_{CO_2} and ΔP .

in low-porosity zones: S_{CO_2} was higher in LPL than in HPL. The reverse correlation is also shown in axial saturation maps between LPL2 and HPL2 in I6 (Fig. 2). Fig. 8 illustrates the correlation between the sectional average of S_{CO_2} and porosity for the stuck and normal-flow zones in run I6. In the stuck zone, residual S_{CO_2} decreases with increasing porosity in each layer, indicating concentrations of the residual CO_2 into LPL, whereas in the normal-flow zone most of the CO_2 in HPL (section porosity larger than 18 per cent) was flushed out by the brine. The larger amount of the residual CO_2 in the stuck zone can be produced by stagnant flow at low-porosity zone ($d = 25\text{--}27.5 \text{ mm}$) where the layers work as a strong barrier against CO_2 flow (Kogure *et al.* 2017). The results will be suggestive for the trapping mechanisms of residual non-wetting fluids in reservoir rocks.

Zhang *et al.* (2014) reported a relationship between pore diameter and normalized pore volume for LPL and HPL of a Berea sandstone sample obtained from the same rock block used in this study (Fig. 9). The largest difference in pore-size distribution between LPL and HPL was found in a pore-diameter range from 0.5×10^{-6} to $5 \times 10^{-6} \text{ m}$ (enclosed in the shaded ellipse in Fig. 9). Pores in this diameter range may act as pore throats which connect larger pores (Zhang *et al.* 2014). Smaller (than $0.5 \times 10^{-6} \text{ m}$) diameter pores are presumably either not connected or do not efficiently transmit viscous fluids. The smaller pore-throat volume in LPL than HPL suggests more dead-end pathways in LPL than HPL because of potentially fewer connected pore-throat networks in LPL. The less connected pore-throat networks and increasing of the pore volume with decreasing of pore diameter may be a cause for increasing of residual gas trapping with decreasing section porosity in the stuck zone after the brine flushing, I6.

In the stuck zone where injection pressure is relatively higher than capillary pressure, CO_2 can be forcibly pushed into narrower pores or pore throats. In drainage run D6, the S_{CO_2} in the stuck zone was around 65 per cent whereas in normal-flow zone it was around 50 per cent (Fig. 7, Table 1). These saturation values correspond to

the maximum capillary pressures of 14 and 7.5 kPa for the Berea sandstone, respectively (Pini & Benson 2013). The capillary pressures squeeze CO_2 into pores of diametres larger than 2.3×10^{-6} and $4.2 \times 10^{-6} \text{ m}$, respectively. The pore diameter of $2.3 \times 10^{-6} \text{ m}$ belongs to the range mentioned above. Displacement of brine by CO_2 in such smaller pores (i.e. Haines jump) was most facilitated during run D6 with the largest capillary pressure. Then, snap-off of CO_2 follows the displacement due to the invasion of brine into a pore throat (Andrew *et al.* 2015).

The average S_{CO_2} in the stuck zone was 5–10 per cent higher than that in normal-flow zone during imbibition (Fig. 7). Since porosity in the stuck zone is lower than in the normal-flow zone, more isolated CO_2 ganglia appeared in the stuck zone. The isolated CO_2 ganglia were encompassed by brine and immobile because high capillary pressure is necessary for displacements. Thus the residual CO_2 mostly consisted of isolated CO_2 ganglia that remain in smaller pores, and their distribution pattern roughly reflects that of S_{CO_2} during drainage although it shows an opposite pattern of the peaks and troughs in the normal-flow zone.

It is interesting to note that the CO_2 saturation in a reservoir can be maintained at about 40 per cent when a small volume of CO_2 still flows (~ 10 per cent CO_2 fraction based on the present results). This indicates that some CO_2 can move away through the connected pathways formed by percolated CO_2 ganglia, and some CO_2 can remain in the reservoir keeping its saturation value about 40 per cent until the spontaneous imbibition by 100 per cent brine. The saturation values of CO_2 are very different between the two-phase flow and the single-phase flow of brine (Table 1).

The above two trapping mechanisms are classified as physical trapping; the former is referred to as structural or stratigraphic trapping whereas the latter is residual gas trapping. The latter is favourable for long-term storage security (Metz *et al.* 2005). Reservoir heterogeneity may control the two trapping mechanisms. Rocks having large pores are favourable for the structural or stratigraphic trapping, whereas rocks that contain large volumes of small pores

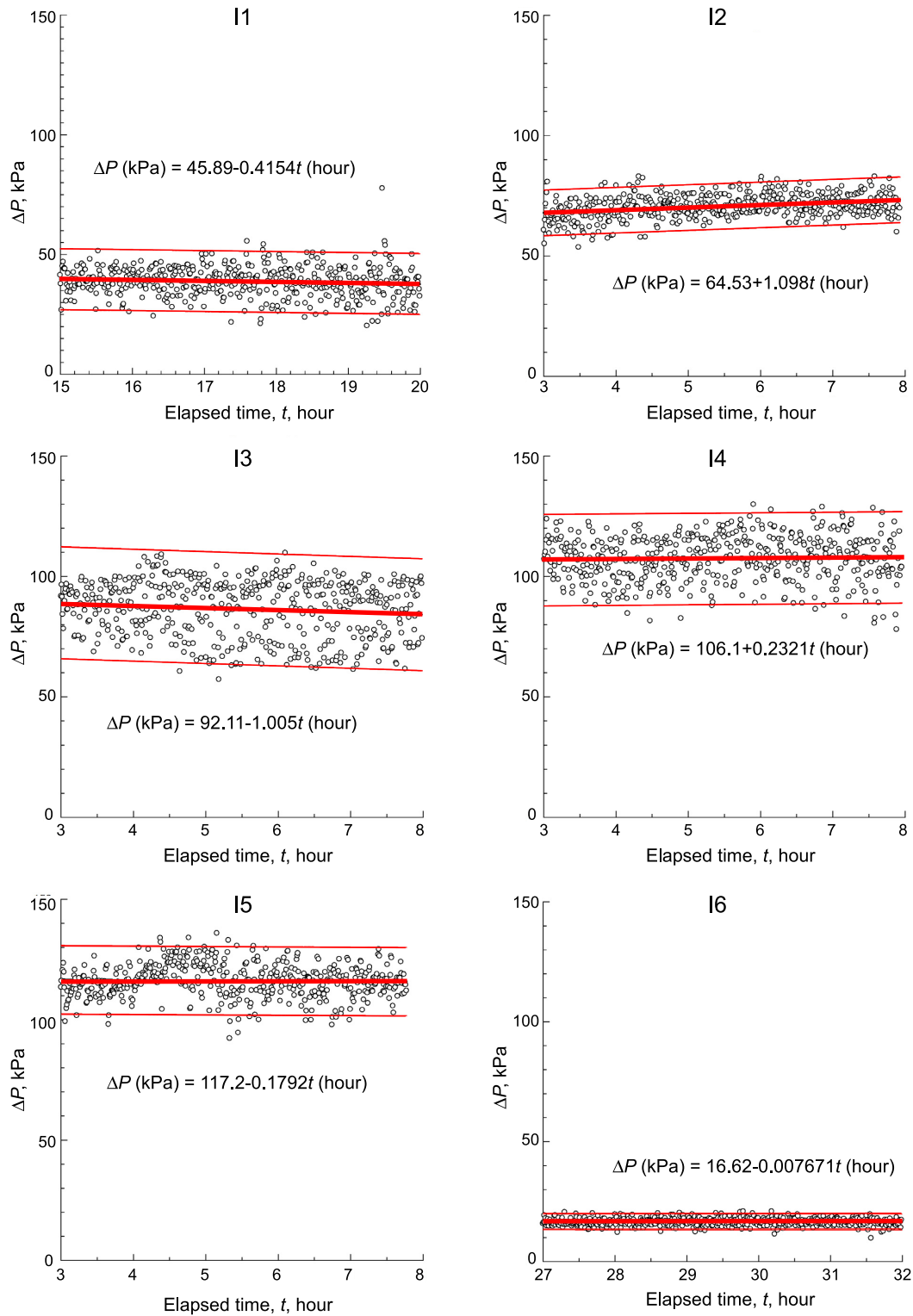


Figure 4. Time variation of ΔP for 5 hr before the end of injection in runs I1–I6. There seem to be linear trends and random fluctuations as shown by the linear regression and 2σ shown by the thick and thin red lines. We used the ΔP at the final value of the linear regression for all calculations in Figs 3 and 10.

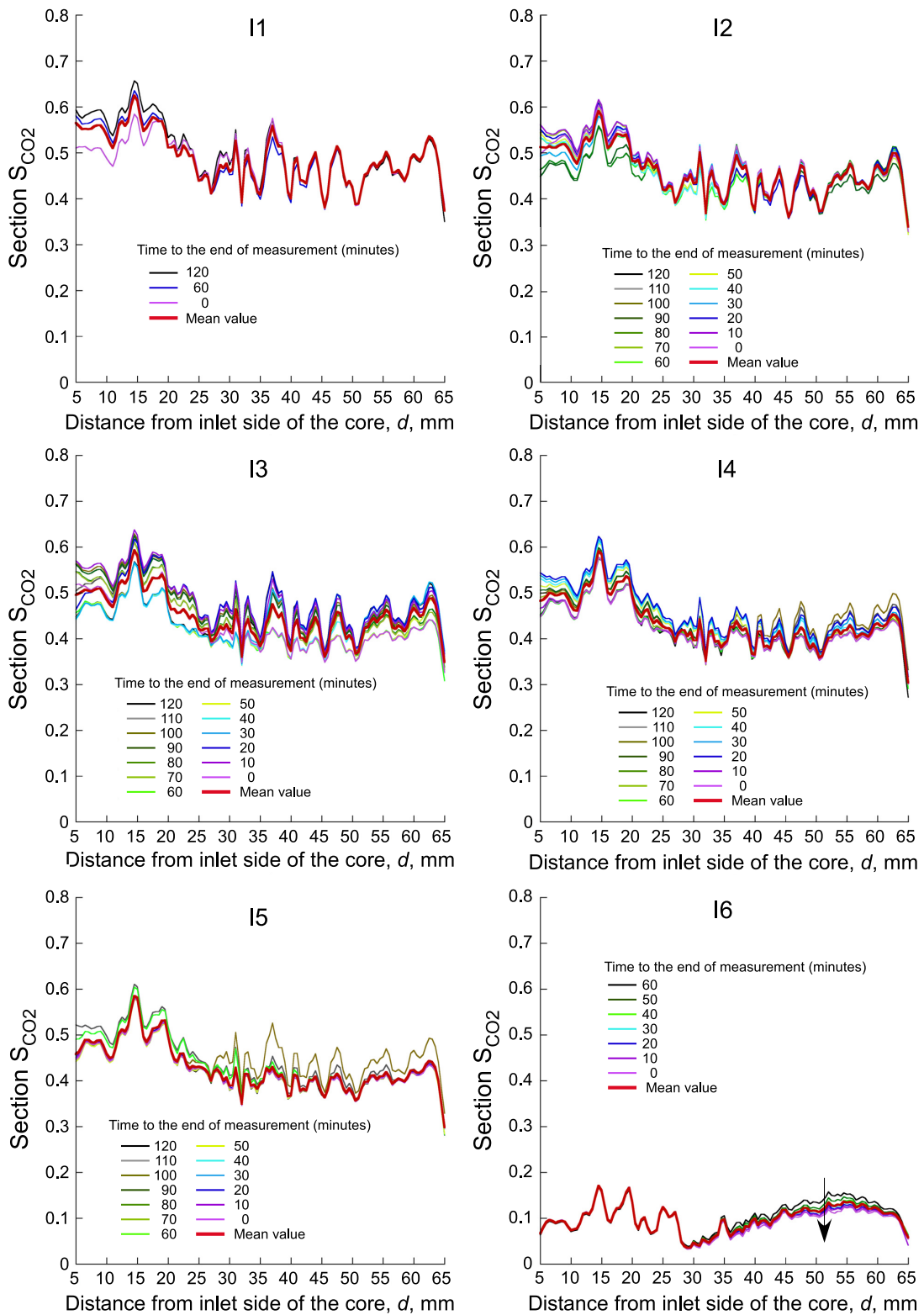


Figure 5. Temporal change in the axial S_{CO_2} profile during the last 2 hr of runs I1–I5 and 1 hr of run I6.

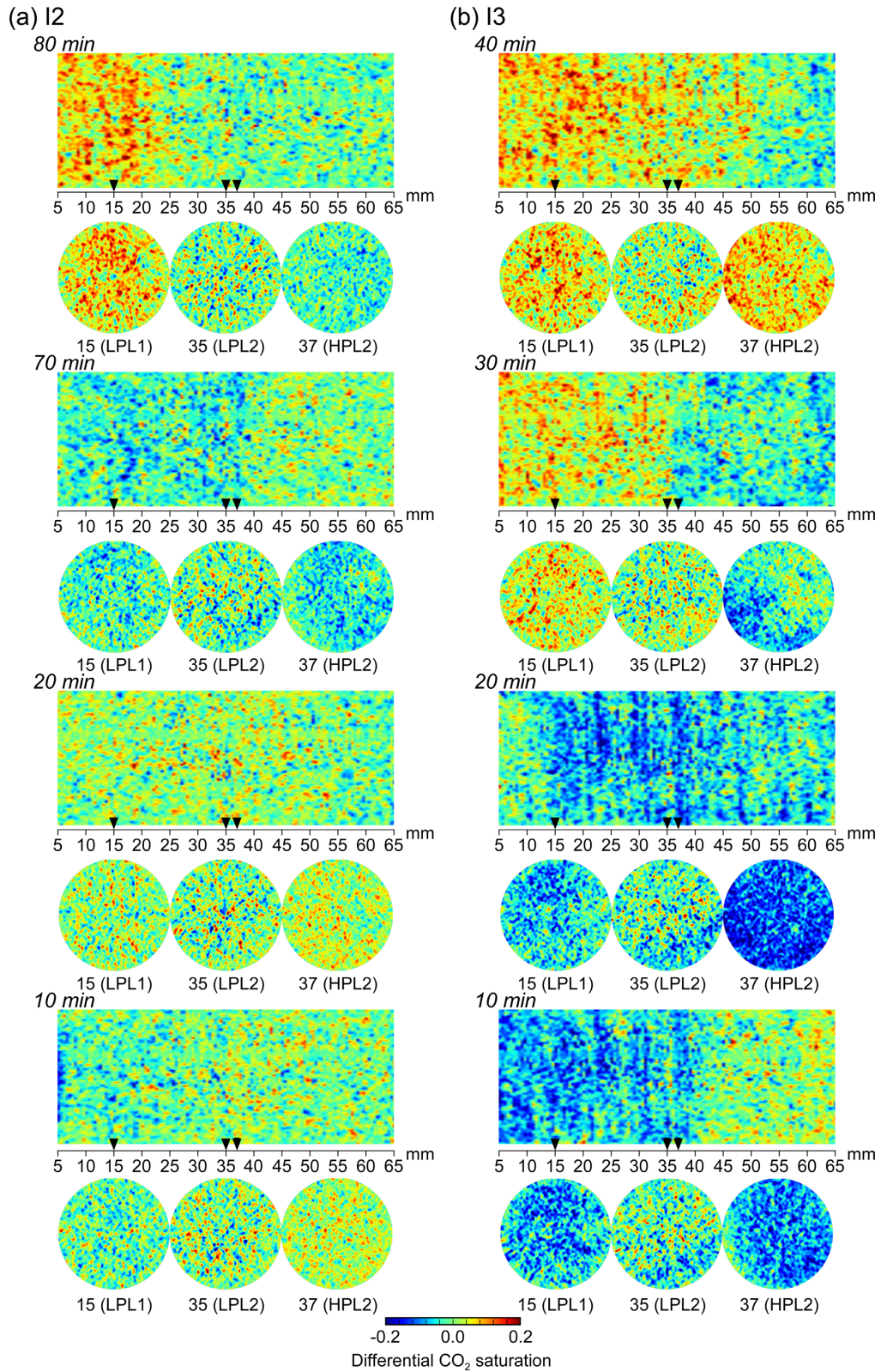


Figure 6. Differential S_{CO_2} maps and sectional profiles along the long axis during runs (a) I2 and (b) I3. The black triangles on the horizontal axis show the locations of axial images. Time from the end of the measurements is noted above each map.

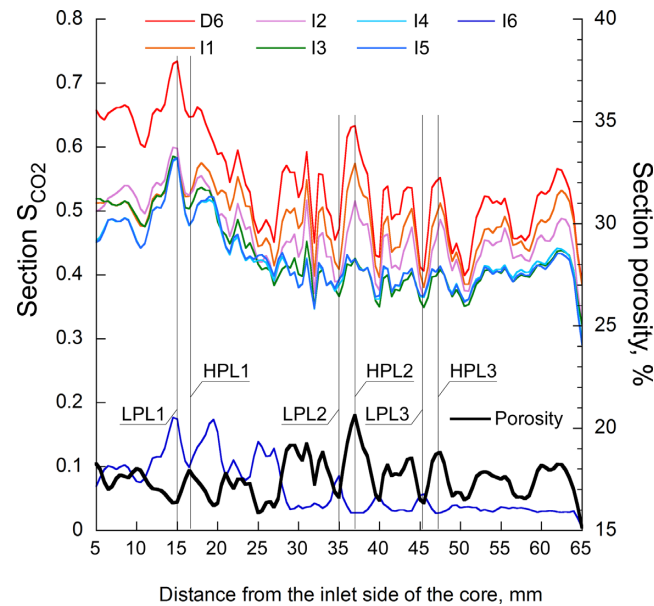


Figure 7. Axial distribution of S_{CO_2} in the seven injection runs: one for drainage (run D6, in Kogure *et al.* 2017) and six for imbibition (runs I1–I6, in this study). Run I6 is for 100 per cent brine imbibition. Axial distribution of porosity (heavy black line) is also shown. The sections denoted by LPL1–LPL3 and HPL1–HPL3 correspond to those in Fig. 1.

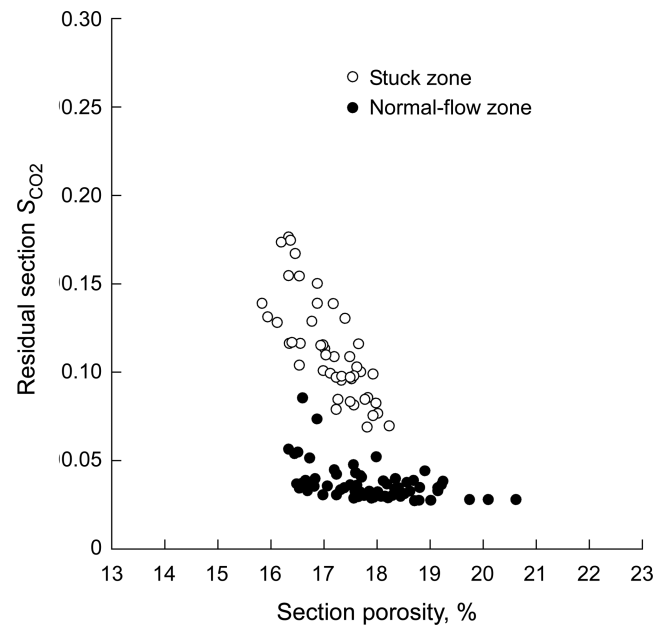


Figure 8. The relationship between sectional average porosity and residual S_{CO_2} at the end of run I6.

are favourable for the residual CO_2 trapping although high injection pressure would be necessary to forcibly squeeze CO_2 into the narrow pores.

6 RELATIVE PERMEABILITY CURVES

Fig. 10 plots RPCs from this study and Kogure *et al.* (2017), showing a slight hysteresis of the RPC in a cycle of drainage and imbibition. Relative permeability of brine and CO_2 , k_{rb} and k_{rCO_2} , were

calculated using Darcy's law by substituting parameters. The values of ΔP used to calculate relative permeability were determined by approximating ΔP for several hours before the end of the measurements (Fig. 4). The values of RPC at the end of runs I1–I6 are shown in Table 1. The value of k_{rb} during imbibition is slightly higher than that during drainage. Akbarabadi & Piri (2013) reported hysteresis of relative permeability for a brine– CO_2 system under steady-state flow conditions, and several experiments using the unsteady-state

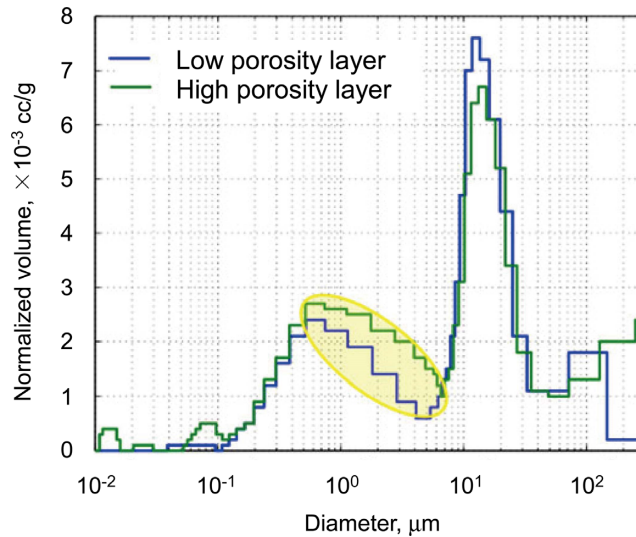


Figure 9. Pore-size distributions of LPL and HPL (modified after Zhang *et al.* 2014). The yellow shaded area shows the difference of pore-throat number (or pore-throat diameter) between the two layers.

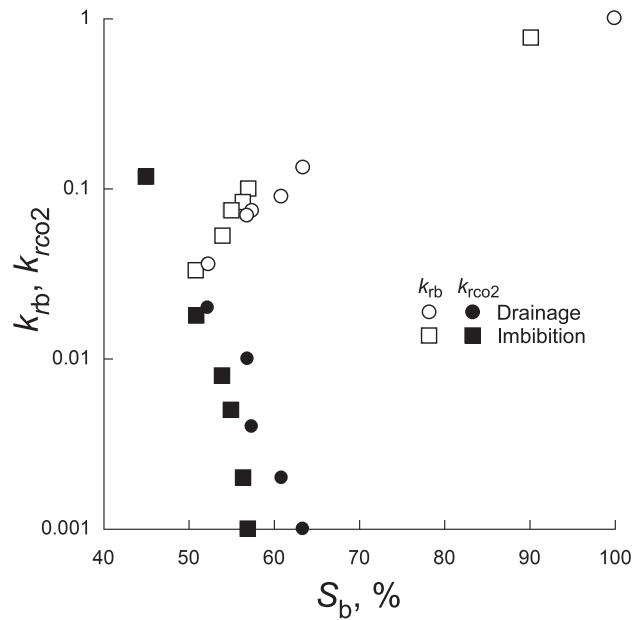


Figure 10. Relative permeability plots from this study (imbibition) and from Kogure *et al.* (2017; drainage).

method also reported hysteresis (e.g. Bennion & Bachu 2007; Akbarabadi & Piri 2013; Soroush *et al.* 2013; Wang & Alvarado 2016). Akbarabadi & Piri (2013) also showed that the relative permeability of brine during imbibition was higher than that during drainage for the brine–CO₂ system in Berea sandstone. The hysteresis observed in this study is small compared to that in Akbarabadi & Piri (2013). Total flow rates of injected fluids were not kept constant through the measurement of RPC in Akbarabadi & Piri (2013). Our study indicates slight differences in RPCs between drainage and imbibition under the same total flow rate and velocity.

Snap-off is caused by decrease in non-wetting phase saturation due to increase in wetting phase saturation, which results in decrease

in the volume of a non-wetting phase ganglia as the ganglia rearrange to find a lower energy configuration allowing wetting phase to fill a pore throat (Singh *et al.* 2017). Singh *et al.* (2017) reported an inverse log-linear relationship between the snap-off event frequency and the brine-filled pore volume at each event in imbibition, and that the brine-filled pore volume is of the order of the average pore volume, which is about 2–3 orders of magnitude smaller than that can occur in drainage. Considering the above relationship between snap-off event frequency and brine-filled pore volume, the smaller brine-filled pore volume in imbibition suggests that there are more snap-off points during imbibition than during drainage. An increase in the number of snap-off points could cause an increase of flow

resistance, which would be reflected by higher differential pressure and larger pressure fluctuation for the same brine and CO₂ fractions during imbibition than drainage. This is also reflected in velocity changes: fragmentation of non-wetting phase ganglia in imbibition have been reported in relation to *P*-wave velocity changes in a drainage–imbibition cycle (Cadoret *et al.* 1995; Nakagawa *et al.* 2013; Zhang *et al.* 2015).

Another possible reason for the relative permeability hysteresis may be related to the porosity distribution of Berea sandstone used in this study. The rock has a bimodal porosity distribution as shown in Fig. 9; the largest peak around 10¹ μm and second largest below 10⁰ μm. Measuring elastic wave velocities in patchy saturated rocks, Le Ravalec *et al.* (1996) showed the difference in flow paths where fluids go through during drainage and imbibition if the rocks have both micro- and macropores. Zhang *et al.* (2015) also reported the changes in distribution pattern of CO₂ between drainage and imbibition in a heterogeneous sandstone core. Therefore, the bimodal porosity distribution can also be the cause of the hysteresis in this study.

7 CONCLUSIONS

Simultaneous injections of brine and CO₂ were performed in Berea sandstone to reveal flow mechanisms of CO₂ and brine during the imbibition process under very low flow velocity conditions mimicking the two-phase flow in a front edge of CO₂ far from an injection well in actual CCS sites. A slight hysteresis of the relative permeability curve was observed in a drainage and imbibition cycle. This may indicate the effect of low flow rate. During the imbibition, oscillatory fluctuations in local CO₂ saturation and differential pressure across the core were observed except for the case of full imbibition, where only brine flows. The degree of the fluctuation became larger when CO₂ saturation decreased to around 40 per cent, which is near the percolation threshold of pore networks for most of sandstones. The oscillatory fluctuations are therefore considered to result from morphological changes of CO₂ pathways due to ganglion dynamics: coalescences of CO₂ ganglia that form CO₂ percolation clusters and their snap-off by brine invasion. Supercritical CO₂ is removed from larger pores and stored in smaller pores during the full imbibition. This suggests that CO₂ at field scales will be preferentially left in low-porosity layers rather than in high-porosity layers during the spontaneous imbibition by aquifer brine, a long time after CO₂ injection.

We consider that recent findings on ganglion dynamics can be successfully applied to interpret the CO₂/brine migration of conventional core-scale experiments made under very low injection rates or small capillary numbers less than 10⁻⁸. Although our medical X-ray CT provides only coarse-resolution images (0.07–0.5 mm resolution), the observed fluctuations in the differential pressure and the CO₂ saturation can be reasonably explained by adopting the percolation theory and plausible mechanisms for morphological transitions in pore networks that comes from ganglion dynamics. Further technical improvements of the μCT such as sampling interval and enlargement of a targeted object will give us more complete understanding of the nature of fluid migration in larger scale with heterogeneity, which can be applied to field-scale fluid migration.

ACKNOWLEDGEMENTS

We acknowledge R. Kranz for valuable comments and suggestions to this manuscript. Data to support this paper are from the Ministry of Economy, Trade and Industry of Japan (METI) under the research

contract ‘Development of Safety Assessment Technology for Carbon Dioxide Capture and Storage’, and may be available through contact with the corresponding author (TK, kogure@riko.shimane-u.ac.jp).

REFERENCES

- Akbarabadi, M. & Piri, M., 2013. Relative permeability hysteresis and capillary trapping characteristics of supercritical CO₂/brine systems: an experimental study at reservoir conditions, *Adv. Water Resour.*, **52**, 190–206.
- Akin, S. & Kovscek, A.R., 2003. Computed tomography in petroleum engineering research, *Geol. Soc. Lond. Spec. Pub.*, **215**, 23–38.
- Andrew, M., Menke, H., Blunt, M.J. & Bijeljic, B., 2015. The imaging of dynamic multiphase fluid flow using synchrotron-based X-ray microtomography at reservoir conditions, *Transp. Porous Media*, **110**, 1–24.
- Argaud, M., Ghouse, H., Straley, C., Tomanic, J. & Winkler, K., 1989. Salinity and saturation effects on shaly sandstone conductivity, in *SPE Annual Technical Conference and Exhibition*, 8–11 October, San Antonio, TX.
- Armstrong, R.T., McClure, J.E., Berrill, M.A., Rücker, M., Schlüter, S. & Berg, S., 2016. Beyond Darcy’s law: the role of phase topology and ganglion dynamics for two-fluid flow, *Phys. Rev. E*, **94**, 043113, doi:10.1103/PhysRevE.94.043113.
- Bennion, D.B. & Bachu, S., 2007. Permeability and relative permeability measurements at reservoir conditions for CO₂-water systems for ultralow permeability confining caprocks, in *Europec/EAGE Annual Conference and Exhibition*, London, UK.
- Cadoret, T., Marion, D. & Zinsner, B., 1995. Influence of frequency and fluid distribution on elastic wave velocities in partially saturated limestones, *J. geophys. Res.*, **100**, 9789–9803.
- Han, M., Youssef, S., Rosenberg, E., Fleury, M. & Levitz, P., 2009. Deviation from Archie’s law in partially saturated porous media: wetting film versus disconnectedness of the conducting phase, *Phys. Rev. E*, **79**, 031127, doi:10.1103/PhysRevE.79.031127.
- Ito, T., Ohbuchi, A., Nakajima, T. & Xue, Z., 2017. Identifying the source of natural gamma-rays in shallow-marine siliciclastic strata and their significance for shale evaluation: a case study of the CO₂ storage aquifer at the Nagaoka site, Japan, *J. Nat. Gas Sci. Eng.*, **46**, 782–792.
- Kogure, T., Zhang, Y., Nishizawa, O. & Xue, Z., 2017. Migration mode of brine and supercritical CO₂ during steady-state relative permeability measurements at very slow fluid flow velocity. *Geophys. J. Int.*, **211**, 1237–1253.
- Le Ravalec, M., Guéguen, Y. & Chelidze, T., 1996. Elastic wave velocities in partially saturated rocks: saturation hysteresis, *J. geophys. Res.*, **101**, 837–844.
- Metz, B., Davidson, O., de Coninck, H., Loos, M. & Meyer, L., 2005. *Carbon Dioxide Capture and Storage, IPCC Special Report*, Intergovernmental Panel on Climate Change Working Group III, Cambridge Univ. Press.
- Nakagawa, S., Kneafsey, T.J., Daley, T.M., Freifeld, B.M. & Rees, E.V., 2013. Laboratory seismic monitoring of supercritical CO₂ flooding in sandstone cores using the split Hopkinson resonant bar technique with concurrent X-ray computed tomography imaging, *Geophys. Prospect.*, **61**, 254–269.
- Perrin, J.-C. & Benson, S., 2010. An experimental study on the influence of sub-core scale heterogeneities on CO₂ distribution in reservoir rocks, *Transp. Porous Media*, **82**(1), 93–109.
- Pini, R. & Benson, S.M., 2013. Simultaneous determination of capillary pressure and relative permeability curves from core-flooding experiments with various fluid pairs, *Water Resour. Res.*, **49**, 3516–3530.
- Rücker, M. *et al.*, 2015. From connected pathway flow to ganglion dynamics, *Geophys. Res. Lett.*, **42**, 3888–3894.
- Singh, K., Menke, H., Andrew, M., Lin, Q., Rau, C., Blunt, M.J. & Bijeljic, B., 2017. Dynamics of snap-off and pore filling events during two-phase fluid flow in permeable media, *Sci. Rep.*, **7**, doi:10.1038/s41598-017-05204-4.
- Soroush, M., Wessel-Berg, D., Torsaeter, O. & Kleppe, J., 2013. Investigating impact of flow rate and wettability on residual trapping in CO₂ storage in saline aquifers through relative permeability experiments, *Energy Environ. Res.*, **3**, 53–72.

- Span, R. & Wagner, W., 1996. A new equation of state for carbon dioxide covering the fluid region from the triple-point temperature to 1100 K at pressures up to 800 MPa, *J. Phys. Chem. Ref. Data*, **25**, 1509–1596.
- Wang, X. & Alvarado, V., 2016. Analysis of capillary pressure and relative permeability hysteresis under low-salinity waterflooding conditions, *Fuel*, **160**, 228–243.
- Wagner, W. & Kretschmar, H.-J., 2008. *International Steam Tables, Properties of Water and Steam*, 2nd edn, pp. 392, Springer-Verlag.
- Zhang, Y., Nishizawa, O., Kiyama, T., Chiyonobu, S. & Xue, Z., 2014. Flow behaviour of supercritical CO₂ and brine in Berea sandstone during drainage and imbibition revealed by medical X-ray CT images, *Geophys. J. Int.*, **197**, 1789–1807.
- Zhang, Y., Nishizawa, O., Kiyama, T. & Xue, Z., 2015. Saturation-path dependency of P-wave velocity and attenuation in sandstone saturated with CO₂ and brine revealed by simultaneous measurements of waveforms and X-ray computed tomography images, *Geophysics*, **80**, D403–D415.
- Zhang, Y., Kogure, T., Nishizawa, O. & Xue, Z., 2017. Different flow behavior between 1-to-1 displacement and co-injection of CO₂ and brine in Berea sandstone: insights from laboratory experiments with X-ray CT imaging, *Int. J. Greenhouse Gas Control*, **66**, 76–84.